



●Original Contribution

3D ULTRASONIC IMAGE FEATURE LOCALIZATION BASED ON MAGNETIC SCANHEAD TRACKING: *IN VITRO* CALIBRATION AND VALIDATION

PAUL R. DETMER,^{†*} GERARD BASHEIN,^{‡*} TIMOTHY HODGES,[†] KIRK W. BEACH,^{†*}
ERIC P. FILER,^{*} DAVID H. BURNS^{*} and D. EUGENE STRANDNESS, JR.[†]

Departments of [†]Surgery and [‡]Anesthesiology, and ^{*}The Center for Bioengineering
at the University of Washington, Seattle, WA, USA

(Received 1 April 1993; in final form 30 March 1994)

Abstract—The basis of a three-dimensional (3D) ultrasound imaging system was constructed from a commercially available magnetometer-based position and orientation measurement (POM) device, a standard B-Mode ultrasound instrument and a personal computer. To evaluate the system's performance, a novel method was devised using an iterative, least-squares technique to simultaneously determine the system's calibration parameters and measure its precision in locating points in three-dimensional space. When tested separately, the POM system located single points with a root mean squared (RMS) uncertainty of from 1.4 mm to 3.2 mm over the 610 mm working radius of the system. When combined with the ultrasound instrument, the RMS uncertainty in locating point targets varied from 2.1 mm to 3.5 mm. These results establish the lower limits of variability to be expected from this system when locating fiducial anatomical landmarks for repeated examinations of the same region of the body, and when making numerical 3D reconstructions from multiple planar images.

Key Words: Ultrasound, Imaging, Three-dimensional, Magnetometer.

INTRODUCTION

Traditional B-mode ultrasound imaging provides two-dimensional (2D) tomographic images of any selected region of the body. Using this method, the examiner must mentally integrate the information obtained from multiple 2D views to appreciate the three-dimensional anatomy. This process requires a great deal of training to achieve proficiency, and is very time consuming. In addition, quantitative analysis is limited to two dimensions, with only qualitative interpretation possible in the third dimension.

To date, three-dimensional (3D) spatial ultrasound imaging has been only partially successful, particularly when compared with other imaging modalities such as x-ray computed tomography and magnetic resonance methods. Despite ultrasound's advantages in generating real-time images and accurately measuring blood flow, the development of ultrasonic tomography

has been limited by the difficulty in rapidly acquiring and combining images taken from multiple viewpoints and angles. One of the difficulties in implementing automated scanning techniques for gathering ultrasound data in three dimensions is maintaining an adequate exchange of acoustic energy between the ultrasound transducer and the body. Unless a water tank or some fluid-filled pillow is used for acoustic coupling, the transducer must maintain direct contact with the body to efficiently transfer acoustic energy. The use of hand-held scanheads equipped with a position locating device has so far been the most popular method for obtaining 3D ultrasound data from a variety of locations in the body.

While earlier investigators have coupled hand-held ultrasonic scanheads with acoustic (King et al. 1991; Levine et al. 1989; Moritz et al. 1983), mechanical (Greenleaf and Bahn 1981; Martin et al. 1990; Nerstrom et al. 1991; Schmitt et al. 1984; Sohn et al. 1988a, 1988b; Steinke and Hennerici 1989), or video position and orientation measurement (POM) systems (Stone 1990; Watkin and Rubin 1989), the complexity and awkwardness of these systems have limited their

Supported by Grants HL42270 and HL41464 from the National Institutes of Health, Bethesda, MD.

Address correspondence to: Paul R. Detmer, Ph.D., Department of Surgery RF-25, University of Washington, Seattle, WA 98195, USA. E-mail: pdetmer@u.washington.edu

use to research. Members of our group found many problems in our earlier experience with the acoustic spark-gap system developed by Moritz et al. (1976, 1977). When using the spark-gap system, the examiner had to ensure that the spark-gap array always faced toward the microphone array above the examining table, which limited the scanhead's orientation to a range of about ± 70 degrees around the vertical. Thus, the scanning of many anatomical locations was severely restricted unless the subjects were placed in uncomfortable positions. Also, some patients did not tolerate the crackle and flash of spark gaps located near the face during neck or chest examinations, and moving air currents in the room would often lead to unstable measurements (Moritz and Shreve 1977).

Potentiometer-based lever arm systems for 3D ultrasound have also been reported in the literature (Moritz et al. 1976), although no accuracy data have been given. These systems would appear to limit the examiner's freedom of movement and range even more severely than the spark-gap systems. Furthermore, as the maximum range of the device is approached, freedom of movement becomes even more restricted. Accuracy would also deteriorate at the limits of range, because angle measurement errors at each joint are magnified by the distance of each limb along the lever arms to the scanhead face. The effect of angle error on position would be compounded over all of the joints and the cumulative length of their arms.

Other mechanical systems have been reported that use translational or rotational carriage systems. Some of these systems were designed for specialized applications, such as breast transmission tomography (Greenleaf and Bahn 1981; Schmitt et al. 1984) or transrectal urethra imaging (Nerstrom et al. 1991). These systems were carefully designed to address their specific imaging problems, and are not applicable to more general vascular, obstetric and cardiac imaging applications. Some mechanical systems are limited to rotation or very limited translation of the scanhead (Sohn et al. 1988a, 1988b; Steinke and Hennerici 1989), by the constraint that the scanhead has to maintain acoustic contact with the body. Other investigators have employed video scene-recording methods to determine the position and orientation of the ultrasonic scanhead (Stone 1990; Watkin and Rubin 1989). These techniques require extensive off-line processing of the video recordings, and operator movement must be restricted to guarantee that the cameras have a clear view of the scanhead at all times. We have found no published evaluations of the accuracy of any of these systems.

Recent technological advances in magnetic POM instruments have made them attractive for clinical 3D

ultrasound. We developed a system for 3D scanning that uses a commercially available magnetic POM instrument with its transmitter attached to the underside of the examination table and the receiver attached to the ultrasonic scanhead. We report here on the *in vitro* validation of this system by a novel method that simultaneously measured both the physical calibration parameters and the system's precision by repeatedly imaging feature points from many different points of view.

METHODS

Background on validation in three dimensions

There can be pitfalls in assessing the precision and accuracy of a 3D imaging system if only solid objects are scanned. For example, a misleading validation of volume measurement can result from compensatory random errors in locating the points defining the volume. The underestimation of an object's volume contributed by points erroneously located to the inside of an object's surface will tend to be canceled by the volume overestimation contributed by points erroneously located to the outside of the surface. Similar difficulties can occur for procedures that calculate the distances between pairs of points in space. Systematic position errors, having the same direction for both points of a pair, will tend to cancel, giving nearly correct distances between the points. Both of these validation procedures could underestimate the 3D system's error.

Our approach to measuring spatial precision avoids these problems by measuring how well the system repeatedly identifies the location of a single point in space, when imaged from many different directions and distances. Because measuring volume, distance and surface area all depend on reliably locating points relative to each other, the precision of locating a single point in space is a more fundamental measure of a 3D system's accuracy, because it allows for identification and correction of systematic errors in system calibration. The remaining error, which is the random variability due to noise in the 3D imaging system, can then be estimated.

The precision and accuracy with which a 3D ultrasound imaging system can locate a feature point in space depends upon: (1) the finite resolution of the ultrasound imaging system; (2) the uncertainty in locating the point within the ultrasonic image; and (3) the uncertainty in identifying the position and orientation of the imaging plane in space. By evaluating the precision of the POM system alone and then in conjunction with the ultrasound system, the contributions of each to the overall position variability could be determined.

The lateral and depth resolution limits of the ultrasound imaging system affect how precisely a point can be located within an imaging plane. The thickness of the ultrasound beam normal to the image plane introduces additional location uncertainty in 3D imaging. The magnitude of the location error caused by beam thickness and lateral resolution limitations, as determined by transducer aperture and focusing, are almost always larger than errors due to depth resolution limitations, whose source is the finite duration of the transmit pulse. Thus, it is likely that beam thickness (which is normally ignored in 2D B-mode imaging) and lateral resolution will dominate the imaging system's contribution to 3D spatial location uncertainty of feature points.

Identifying the location of feature points within the ultrasound image plane can be done manually or by using automated computer techniques. Either method will be limited by lateral and depth resolution uncertainty. Additional location error can be introduced by signal dropout, beam refraction and speckle noise. Although manual feature location is subject to reproducibility errors not present in automated techniques, it is often more accurate because a human can make more complex decisions about difficult regions. Because the feature-to-background contrast and noise can be carefully controlled in an *in vitro* environment vs. *in vivo*, both manual and automated methods will generally perform much better in *in vitro* experiments.

The method used to identify the position and orientation of the image plane in space will also introduce error in locating a point. The position errors in locating the ultrasonic scanhead will add directly to the other errors, but errors in determining the orientation of the image plane will affect overall location error in a less obvious manner. Figure 1 summarizes the effect of orientation uncertainty on the 3D spatial location of a point in the image plane. The contribution of a given orientation error to location error depends upon the distance of the feature point from the position-locating device. This source of error can be reduced by attaching the position-locating device as close as possible to the face of the scanhead, provided it does not interfere with the operator's manipulation of the scanhead (see Fig. 2).

To locate a feature point in space, the POM system must furnish both the location and orientation of the 2D coordinate system of the imaging plane relative to a fixed frame of reference. Figure 3 summarizes the relationship between the coordinate systems of the image plane, the scanhead/receiver assembly and the examining table's global frame of reference, as defined by the transmitter. However, the situation is complicated because, in our chosen POM system, the origins

of the receiver's and transmitter's axes are contained within the respective devices and are not indicated by any external landmarks. Because the system reports the relative positions of the transmitter and receiver, determinations of the locations of the origins with respect to each other or to external landmarks can be made, but will be limited in accuracy by the position error inherent in the locating system, *i.e.*, one of the quantities that we want to measure. By using the technique of repeatedly measuring the location of a single point in space with respect to the transmitter, using multiple receiver positions and orientations, it becomes possible to estimate simultaneously the system's error *and* the location of the receiver and transmitter's coordinate systems.

Apparatus

Our 3D imaging system uses a commercial ultrasound scanner (Ultramark-9 HDI, Advanced Technology Laboratories, Bothell, WA, USA) and a pulsed magnetic field position and orientation measurement system (Bird Model 6D-BRD, Ascension Technology Corp., Burlington, VT, USA) attached to a scanhead. The particular scanhead used in this study was a 7.5 MHz hand-held linear HDI scanhead, although any other could be used. Full frame (two field) ultrasound images from the video output of the ultrasound scanner were directly digitized in 33 ms by a frame grabber board (PCVision Plus, Imaging Technology Inc., Bedford, MA, USA) installed in a personal computer (IBM model AT desktop computer, IBM Corp., Boca Raton, FL, USA) operating under custom software control, which subsequently saved the image and POM data to a hard disk. Figure 4 is a block diagram of the system. Two video monitors allow simultaneous viewing of the image directly from the ultrasound instrument and after digitization and addition of video overlays. The overlays can numerically display absolute position and orientation (see Fig. 8), or graphically aid in visualizing the spatial relationship between the current image plane and previously captured images. Off-line analysis of the digitized images to identify locations of feature points and scale factors was performed with the aid of a trackball on the same computer using custom software. Numerical calculations were performed using PC-MATLAB (The Mathworks Inc., Sherborn, MA, USA).

An RS-232 serial connection, operating at 19 200 baud, allows the computer to update the position and orientation of the scanhead from the POM system every 13 ms. Each selected digitized image and the corresponding scanhead's position and orientation are written to a single data file, ensuring that the image data

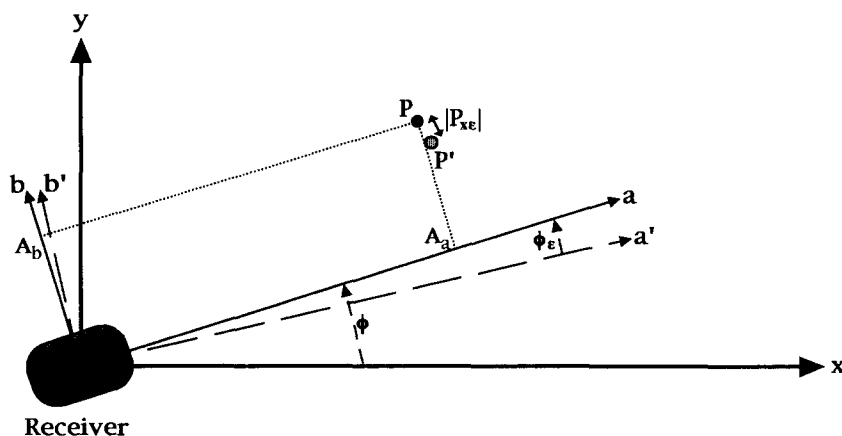


Fig. 1. Error in estimating the true position of a point **P**, when there is an error ϕ_e in the receiver's reported orientation angle, ϕ . In the 2D case shown, with the receiver at the origin of the transmitter's coordinate system, the x -component of the point's true position is $P_x = A_a \cos \phi - A_b \sin \phi$. The x -component of the noisy position estimate is $P'_x = A_a \cos(\phi + \phi_e) - A_b \sin(\phi + \phi_e)$. The x -component of the position error is: $|P_{xe}| = \sin \phi_e (A_a \cos \phi - A_b \sin \phi)$. If the distance **A** from the receiver to the point is increased, this position error gets proportionally larger. Thus, the receiver should be located as close as possible to the target point.

and corresponding spatial information always remain together.

The POM system is based on a pulse-flux magnetometer and consists of an electronic system control unit, a transmitter and a receiver. The position and orientation of the receiver are tracked by the control unit relative to a point within the transmitter, which emits three orthogonal magnetic fields. The three fields are pulsed in sequence. When the first pulsed field is "on," the control unit senses the field strength at the receiver in three orthogonal directions. This process is

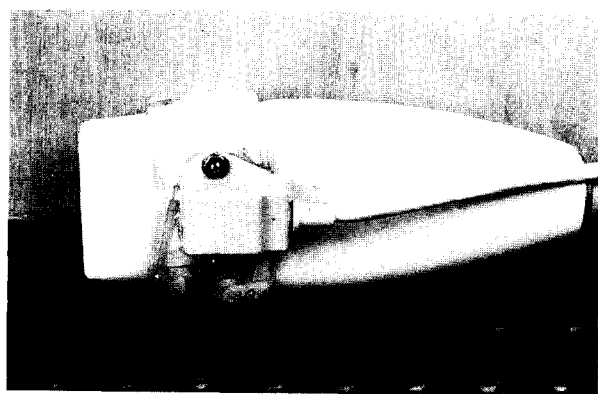


Fig. 2. Photograph showing the mounting of the POM receiver on a linear array scanhead. The receiver is small and lightweight, and it is positioned so as not to interfere with maneuvering the scanhead during examination, while keeping it as close as possible to the image plane to minimize angle error effects. Because the receiver is a sealed unit, it is difficult to accurately measure the exact location of the origin of its coordinate axes.

repeated for the transmitter's other two field coils. An additional receiver sensing cycle is performed with no fields generated by the transmitter to measure the background field strength. The relative strengths of all three pulsed magnetic fields are compared, after subtracting the background field strength, to determine the distance and orientation of the receiver's axis system with respect to the transmitter's. The distance is reported as the x , y and z location of the receiver's axis origin with respect to the transmitter's origin. The orientation is reported as a matrix of angle cosines. Each angle cosine value gives the unit vector projection of a receiver's axis (a , b or c) onto the transmitter axis (x , y or z). Thus, twelve values describe the receiver's position and orientation with respect to the transmitter.

Procedures

To measure the POM system's precision, independent of the resolution limits of the imaging system, the receiver/scanhead assembly was mounted on a wood base with a small spherical bead attached to one corner of the base, 17 cm from the POM system's receiver (see Fig. 5). The bead was then placed in a hole of a sheet of pegboard (whose holes were on one inch (25.4 mm) centers) mounted on the wooden examination table along with the POM system transmitter. This arrangement allowed the receiver/scanhead/base assembly to be rotated relative to the transmitter, around a single point in space, as defined by the center of the bead. The spatial data from the POM receiver was obtained for a minimum of 33 different nearly uniformly distributed receiver positions and ori-

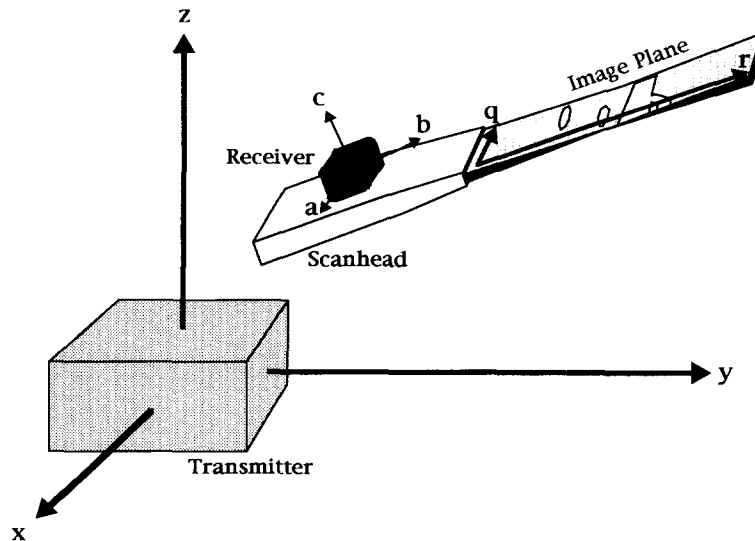


Fig. 3. Diagram of the relationship between the axis systems of the image plane generated by the scanhead, the POM receiver attached to the scanhead, and the POM transmitter attached to the examination table. The image plane row and column axes (r , q) are mapped into the receiver's axes (a , b , c) using a matrix determined by the calibration procedure. The receiver's axis system is then mapped into the transmitter's axes (x , y , z) by the data supplied by the POM system itself. This allows determination of the location of any row-column address in an image plane in the transmitter's axis system.

entations in the hemisphere swept out around the point. This procedure was repeated with the bead at nine different positions relative to the transmitter's origin.

An iterative least squares procedure, outlined in Fig. 6 and described in detail in the Appendix, was used to determine the location of the bead's center

relative to both the transmitter and the receiver, using the POM system measurements. The procedure begins with a guess of the location of the bead with respect to the receiver. Using this guess and the POM system data, an estimate of the bead's location with respect to the transmitter is made for each sample measure-

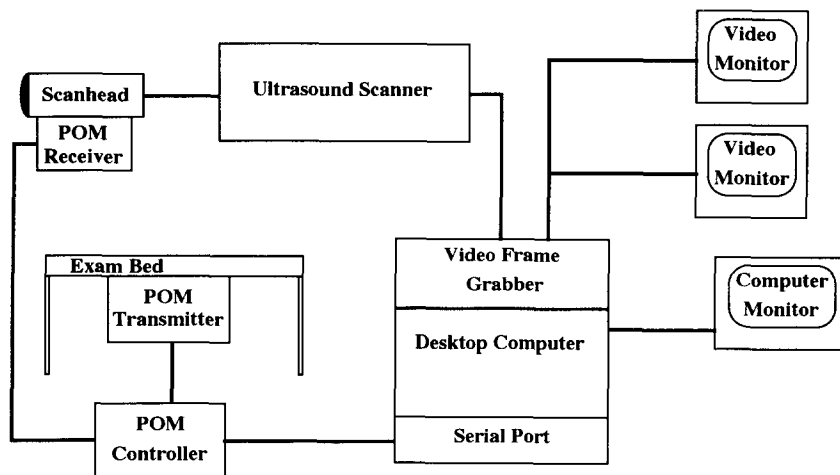


Fig. 4. A hardware block diagram of the 3D ultrasound system. Images are digitized directly from the video output of the ultrasound instrument. At the same time, the POM system measures the location and orientation of the scanhead, and thus each image plane, relative to the examination table. These data are saved along with the digitized image on a disk. Two monitors are available, one to view the unprocessed ultrasound image and the other to view the digitized image, along with overlays showing either the raw position and orientation data (see Fig. 8) or the relative position of the current image plane with respect to previously saved images.

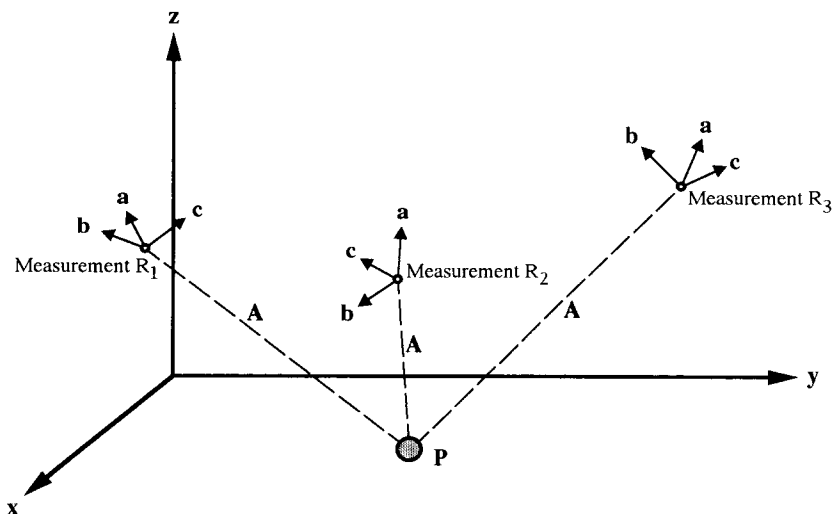


Fig. 5. Diagram illustrating multiple location measurements of a single point P . The receiver, denoted by the a , b , c axes, is attached to the side of a wooden board. A plastic bead is attached to one corner of the board at a distance A from the receiver. The bead is placed in a pegboard hole on the examination table, and the receiver is rotated to many different positions and orientations (e.g., R_1 , R_2 and R_3 as shown) around P . A measurement of the receiver's location and orientation in the transmitter's x , y , z axis system is obtained at each measurement site. The bead is located at a fixed (but unknown) position, P , in the transmitter's axis system and A is a fixed (but unknown) distance between the receiver and the bead. An iterative procedure is used to estimate simultaneously the location of P and the distance A , leaving only measurement noise from the POM system as the uncertainty in estimating the location of P .

ment. A revised estimate of the bead's location in relation to the receiver is calculated that minimizes the vector sum of the x , y and z variability components around the mean x - y - z location of the bead with respect to the transmitter. The algorithm then uses the revised estimate of the bead's location in receiver coordinates to calculate a new estimate of the bead's location in

transmitter coordinates, and so on. The iteration continues until successive changes in the variability of the bead's location in transmitter coordinates cease, within a given tolerance, for successive iteration steps. The standard deviations of the x , y and z components of the bead center's location relative to the transmitter after the final iteration are used as a measure of the precision of the POM system. The vector sum of these standard deviations gives the RMS uncertainty of the POM system. The correlations between the x , y and z error components around the mean were measured to determine whether they were independent of each other.

Because our POM system is based on magnetic field measurement, stray magnetic fields due to operation of the ultrasound system could affect its performance. To test this effect, the isolated POM system test described above was repeated with the POM receiver mounted on the scanhead and the ultrasound system switched off or running in one of three operating modes: B-mode imaging; duplex Doppler or color Doppler imaging. The receiver/scanhead assembly was mounted approximately 11 cm from the bead on the wooden base for this series of measurements.

The point target used for testing the overall 3D ultrasound imaging precision was the intersection of two cotton strings, crossed in a nonplanar X-formation

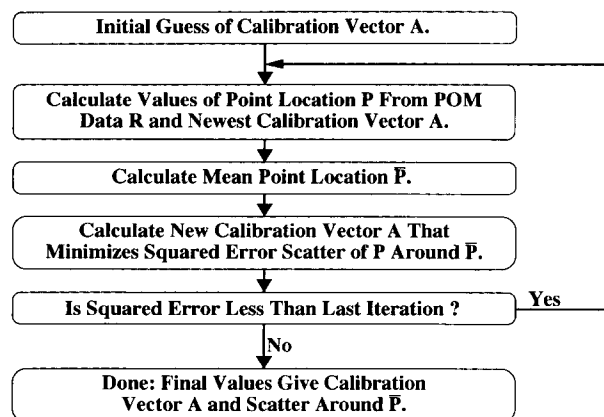


Fig. 6. A flowchart of the algorithm used to calculate the error in estimating the location of a point P and determine the fixed calibration vector A from the receiver to the point P . The mathematical details of the algorithm are given in the Appendix.

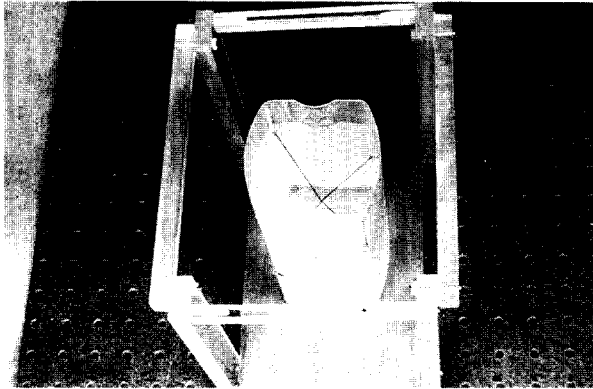


Fig. 7. Photograph showing the crossed string phantom as viewed from the top. Attenuation and distortion of the ultrasound signal by the polypropylene bottle was negligible, allowing images to be obtained from side approaches as well as the top. The bottle was attached to a platform fitted with pegs that held the phantom firmly in place during imaging, but allowed it to be positioned at different points on the surface of the wooden examination table. The height of the crossed strings above the table surface was fixed.

and mounted in a small water tank (see Fig. 7). The base of the tank was fitted with pegs, which held it firmly to the pegboard on the examining bed, while allowing it to be positioned at different locations relative to the transmitter. The small water tank allowed the scanhead to image the intersection point from every approach (except from directly below the bed) at depths from 4 to 6 cm. Transmission of ultrasound through the polypropylene walls of the tank introduced no measurable image distortion in the depth or lateral direction.

From 37 to 41 images of the crossed-string target, each with its corresponding receiver position and orientation, were obtained from different viewpoints around the target. Figure 8 shows an ultrasound image of the string target. By monitoring the echoes of the strings coming together and separating as the scanhead was rocked, the crossing point of the string target could be centered within the thickness of the ultrasonic beam. The thickness of the image plane is evident from the extent to which the individual strings are still visible as they continue away from the centered crossing point, with similar echo strength for two to three millimeters. Afterwards, the row-column location of the string crossing in each image was identified manually, converted from pixels to millimeters and corrected for the speed of sound in water. These locations and the receiver's position and orientation data were analyzed using an enhanced version of the iterative algorithm described above.

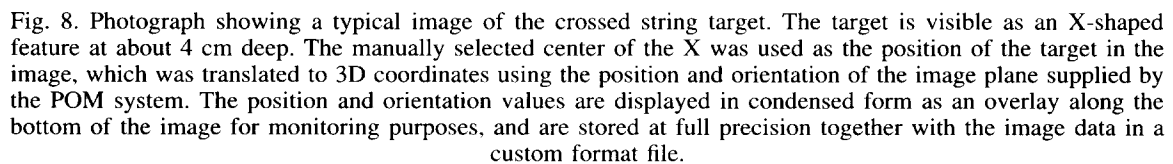
It was necessary to modify the algorithm to accommodate the fact that the location of the string target

with respect to the receiver was not fixed for each image, as was the case in locating the bead target with the POM system alone. Additionally, because the string target could be found anywhere in the plane of the ultrasound image, the orientation of that plane with respect to the receiver's axes also had to be determined by the algorithm. Furthermore, constraints had to be introduced to ensure that the image's row-column axis system remained orthogonal and properly scaled when mapped into the receiver's axis system. The mathematical details are outlined in the Appendix. The enhanced algorithm searched for the position *and* orientation of the receiver with respect to the scanhead's image plane by minimizing the vector sum of the x , y and z components of the scatter around the mean position of the string target with respect to the transmitter.

Two independent sets of 39 ± 2 string target images were obtained at each of four different positions relative to the transmitter. The first set was used to calculate the receiver/scanhead position and orientation data using the iterative algorithm, effectively calibrating the system. The second image data set was then used to calculate the mean and standard deviation of the string target's location. To establish independence of the x , y and z scatter components, correlation coefficients were calculated for the errors, x vs. y , x vs. z and y vs. z . The vector sum of the standard deviations of the x , y and z locations was calculated, giving the overall RMS location uncertainty. A Kolmogorov-Smirnov test was performed to determine whether the data variability around the mean location is consistent with a normal distribution, indicating that the standard deviation could be used as a reasonable measure of the data scatter.

RESULTS

Figure 9 is a histogram showing the variability around the mean position of the x , y and z components of the bead's position for 37 receiver locations. The dashed lines indicate an overall RMS uncertainty of 1.4 mm around the mean bead location. The standard deviations of the variability around the mean location were 0.7 mm, 0.5 mm and 1.1 mm for the x , y and z components, respectively. Figure 10 shows that the RMS location uncertainty increases slowly as a function of distance between receiver to transmitter, until the distance exceeds the specified 610 mm (24 inch) range of the system. Within the rated 610 mm range of the POM system, the RMS uncertainty averaged 2.5 mm. These results compare favorably with the manufacturer's accuracy specifications of 2.5 mm RMS in translation and 0.5 degrees RMS in angle. The components of the location variability correlated with coeffi-



The RMS location uncertainty increases when the feature point is located farther from the receiver. The RMS uncertainty was 1.2 mm when the receiver was located 10 cm from the bead on the wood base, whereas values of 1.4 mm and 2.0 mm were obtained when the receiver was located 17 cm from the bead, indicating that the uncertainty increased about 0.1 mm for every centimeter of separation between the bead and the receiver. These measurements were obtained with the bead positioned between 9 and 11 cm from the transmitter with the ultrasound system switched off.

Table 2 shows the results of locating the string target with the independent sets of image data, using the mean scanhead transformation matrix given in Table 1 as the system calibration. The mean positions of the string target for the four individual data sets are given, along with their standard deviations and maximum ranges around the mean. Figure 11 shows a histogram of the variability around the mean of the x , y and z components of the string target location for all four data sets combined. The dashed lines in the histogram enclose the combined RMS location uncertainty of 3.0 mm in estimating the target's location. The Kolmo-

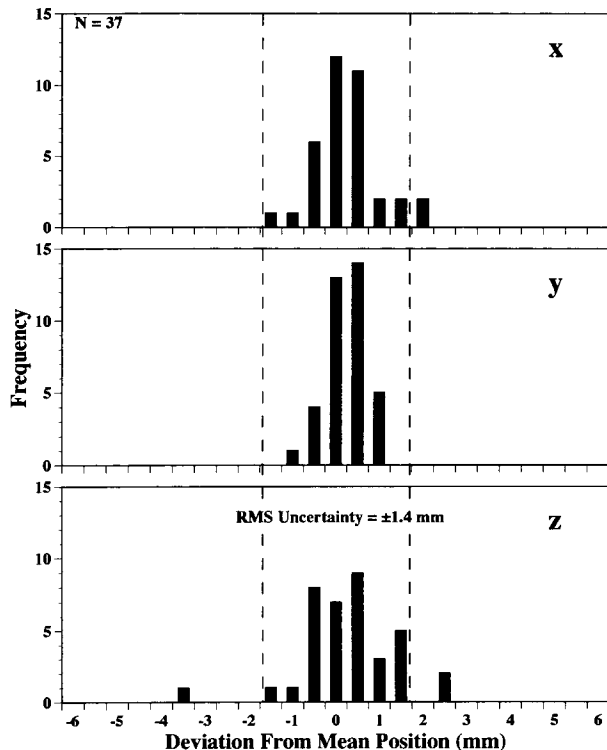


Fig. 9. Histogram showing the x , y and z variability in locating a single point for the isolated POM system. Histogram bins are 0.5 mm wide. The standard deviations of the variability around the mean location were 0.7 mm, 0.5 mm and 1.1 mm for the x , y and z components, respectively. The point was located 103 mm from the POM transmitter and 173 mm from the receiver. The dashed lines show the overall RMS uncertainty range around the mean location of ± 1.4 mm.

gorov–Smirnov test found no significant difference between the data's distribution and a normal distribution, indicating that the standard deviation is a reasonable measure of the location uncertainty. The spatial component variability correlated with coefficients of -0.09 , -0.31 and -0.04 for the x - y , x - z and y - z components, respectively. Only the x - z component correlation is statistically significant ($p < 0.001$), indicating that a relationship between the two components remains after the algorithm iterations have stabilized.

DISCUSSION

This study has demonstrated that precise spatial location of fixed feature points can be accomplished using a 3D ultrasound imaging system based upon magnetic position and orientation measurement. The experimental and computational method that we have presented simultaneously determines the calibration factors of the measurement system and the residual

random error after calibration. By measuring the precision of the POM system independently from the ultrasound system, it was possible to determine the separate contributions of the two major subsystems to the overall position uncertainty.

The reliance of the POM system on its generated magnetic fields makes it susceptible to distortions in that field due to any magnetic or electrically conductive objects, stray magnetic fields and electromagnetic noise in the measurement area. Several steps have been taken in the design of the system and its location to reduce these effects. The table we used for *in vitro* experiments and subsequent patient examinations is constructed from wood, using brass hardware. The receiver is attached to the scanhead with brass screws, plastic and glue. The manufacturers use a null field cycle to remove the effects of any constant or slowly changing magnetic fields from the receiver coil measurements. Additionally, a software adjustable averaging filter is built into the system to control its dynamic response. The filter can be set to reject or accept rapid changes in position and orientation, depending on the application and local noise environment. They also supply a pickup coil with the system that can be plugged into the control electronics and placed near a CRT (or any other periodic electromagnetic noise generator). A special software command forces the system to synchronize its measurement cycle to a consistent point in the noise cycle.

The results we obtained when comparing the precision of the POM system while the ultrasound instru-

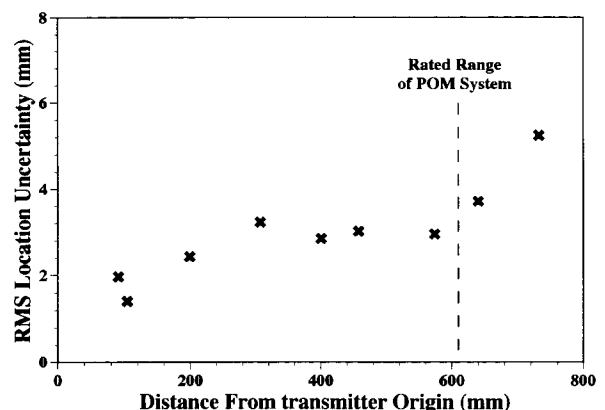


Fig. 10. Plot revealing the precision of the POM system in isolation as a function of its effective range. The vertical axis is the RMS uncertainty around a point's mean location estimated from multiple receiver locations. The horizontal axis is the point's vector distance from the transmitter's origin. The system's accuracy drops off slowly until its rated range of 610 mm is exceeded. The receiver was maintained at a constant 170 mm away from each single point, exaggerating angle error effects.

Table 1. Values of the scanhead-to-image-plane transformation matrix components determined from the iteration algorithm at four separate locations of the string target.

Value	Set 1	Set 2	Set 3	Set 4	Mean	St. Dev.
S_a (mm)	40.6	39.8	40.7	41.2	40.6	0.6
S_b (mm)	-4.4	-2.7	-3.1	-0.9	-2.8	1.4
S_c (mm)	27.5	26.2	25.1	27.1	26.5	1.1
S_{ra}	1.0	1.0	1.0	1.0	1.0	0.0
S_{rb}	0.0	0.0	0.0	-0.1	0.0	0.1
S_{rc}	0.0	0.1	0.1	0.1	0.1	0.1
S_{qa}	0.0	0.0	0.0	0.0	0.0	0.0
S_{qb}	-1.0	-1.0	-1.0	-1.0	-1.0	0.0
S_{qc}	0.0	0.1	0.1	-0.1	0.0	0.1

See Appendix for definitions of the various components.

ment was turned off or operating in one of several modes, indicates that there is no effect due to induced fields from the signals in the scanhead, or any metal parts within the scanhead. All experiments were performed with the ultrasound instrument within one half meter of the POM system with no observable noise and no loss of precision. Because of this, we chose not to use the noise synchronization option or reduce the dynamic response of the system. Some preliminary experiments we performed with the POM receiver temporarily mounted on the back of a mechanical sector scanhead (Access 10PV, Advanced Technologies Laboratories, Bothell, WA), indicated that electromagnetic noise generated by the scanhead motor was not seriously affecting the POM system measurements.

The uncertainty of the POM system increases very slowly with distance within its 610 mm specified range, before degrading smoothly beyond this range. We suspect that some of the observed uncertainty in evaluating the POM system alone may have been due to inconsistency in seating the bead on the base holding the POM receiver into the pegboard hole, particularly for

the data points having the larger deviations in the z -component. Lack of uniform sampling by the receiver around the z -component of the bead's position, due to

Table 2. Mean x , y and z components of the string phantom's location relative to the transmitter's origin, along with their standard deviations and ranges around mean location.

	Set 1	Set 2	Set 3	Set 4
Mean x location (mm)	220.4	-87.5	217.6	83.8
Mean y location (mm)	7.2	17.7	-169.9	-130.2
Mean z location (mm)	187.1	181.5	185.2	184.7
St. dev. around mean x (mm)	1.6	1.3	1.6	1.6
St. dev. around mean y (mm)	1.8	1.6	2.4	1.9
St. dev. around mean z (mm)	1.7	1.1	2.5	1.2
Range around mean x (mm)	6.8	5.3	7.2	5.9
Range around mean y (mm)	7.5	6.0	10.0	8.3
Range around mean z (mm)	7.4	5.1	9.8	4.8

The measurements were made using the mean values of the transformation matrix in Table 1. The range was calculated as the difference between the maximum and minimum deviations from the mean.

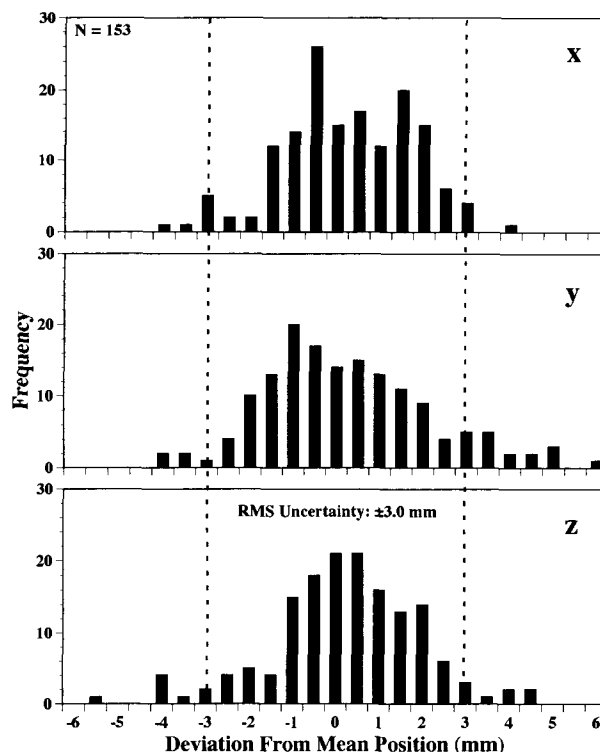


Fig. 11. Histograms showing the x , y and z variability around the mean location of the string target for the combined POM and ultrasound systems. The standard deviations of the variability were 1.5 mm, 1.9 mm and 1.7 mm for the x , y and z components, respectively. Histogram bins are 0.5 mm wide. The overall RMS uncertainty (the dashed lines) was ± 3.0 mm. This is the uncertainty of locating a single point in space from any approach for the entire 3D ultrasound system. It includes effects due to the measurement error of the POM system, the limitations of ultrasound resolution and beam thickness and the error in manually selecting a feature point in an image.

the limits imposed by the plane of the pegboard, may also have contributed to this increased uncertainty in z . When the combined POM and ultrasound systems were evaluated, a more uniform distribution of uncertainty in the x , y and z components was observed, indicating that the POM system does not have a direction-dependent uncertainty. Because the image data used to evaluate the combined systems was collected from a wide range of orientations and approaches, including angled approaches from below the target, the ultrasound system could not compensate for the increased z variability.

Our results clearly demonstrate the importance of mounting a POM device as close as possible to the imaging plane where the 3D coordinates of interest are located. Magnification of the angle uncertainty increases a point's location uncertainty by 0.1 mm for each centimeter between the point and the receiver's origin. This uncertainty is in addition to the receiver's location uncertainty due to system noise and magnetic field distortions. Thus, the 3D location of deeper tissue structures will have inherently higher uncertainty than more proximal structures even before the effects of the ultrasound imaging system are accounted for.

Addition of the ultrasound instrument to the POM system produced an approximate doubling of the estimated position uncertainty over that of the POM system alone. The major contributors to this increased uncertainty appear to be the lateral resolution and beam thickness of the ultrasound instrument and errors in manually locating the point target within the image. Our use of a crossed string imaging target (rather than a ball target) allowed the target to be approximately centered within the thickness of the scanhead beam, and simplified manual location of the precise point in the image where the strings crossed. Significant contribution to position uncertainty was introduced when the target was not accurately centered in the beam. We believe that this approach is a realistic test of the 3D imaging system's performance in localizing anatomic features because the scanhead was hand-held, and because, in practice, the operator would adjust the position of the feature in the scanhead's beam so as to maximize the image quality. Our experimental results reflect a best-case situation, because identifying a string target imaged in water is generally easier than precisely locating anatomic features in tissue.

The depth (axial) resolution of clinical ultrasound systems is much better than their lateral resolution or beam thickness. Thus, depth resolution errors probably do not add significantly to measurement uncertainty, suggesting that the best 3D representation of the image of a surface will be obtained when the scanhead is oriented so that the ultrasound beam intersects the sur-

face in a nearly perpendicular direction. When imaging for purposes of calculating volume, surface area or length, one must keep in mind how the variabilities of the different system components will affect the precision of locating data points. Groups of feature points obtained from a single image plane will have identical POM system data, but their 3D position uncertainty will vary over the image plane due to the changes in the lateral resolution, beam thickness and the accuracy of image feature extraction. High density linear array scanheads, such as the HDI scanhead we used, can perform dynamic focusing, which improves lateral resolution at specific depths, but does not improve the thickness of the beam profile. In contrast, mechanical sector scanheads use circular transducers in an annular array configuration, resulting in a circularly symmetric beam profile with identical resolution in the lateral and thickness directions. All scanheads exhibit beam divergence beyond the focal zone, resulting in resolution degradation in both the lateral and beam thickness directions. Additionally, the POM system's orientation uncertainty generates an increasing position uncertainty the further one gets from the receiver. Thus, when designing a protocol for measuring anatomic features, it would improve accuracy if the features of interest were positioned to be in or near the same image plane and close to the scanhead.

Few studies have been reported that validate the precision or accuracy of other 3D ultrasound systems. Moritz *et al.* (1976, 1977) measured the accuracy of their spark-gap system in isolation, but not in combination with an ultrasound system. King *et al.* (1991) measured the volume and linear distance measuring accuracy of their spark-gap system on a pin model. They reported a standard deviation of 0.66 to 1.26 mm for the error in linear distance measurements, but their experimental technique removed all beam thickness effects by carefully aligning each image plane with the pin targets and in parallel with the other image planes. Thus, their inter-image 3D variability figure is probably somewhat optimistic. Martin *et al.* (1990) measured the distance between steel ball targets in a water tank to evaluate their 3.5 MHz multiangle transesophageal 3D imaging system. They reported an RMS uncertainty of 3.4 mm in the distance between two balls imaged in different planes, averaged over the entire range of the system. This distance uncertainty appears similar to ours.

Among the advantages of the magnetic POM system over other scanhead position sensing systems is that it imposes no limitations on the position and orientation of the scanhead, save that the scanhead/receiver assembly not be moved beyond the 610 mm radius system range. When a patient is placed on the examin-

ing table in a proper position with respect to the transmitter, complete organ and peripheral vascular examinations can be performed within these limitations. We are currently evaluating the system for studying the carotid artery and saphenous vein bypass grafts. Additionally, the manufacturer has recently developed an extended range system claimed to be capable of nearly equivalent performance to a range of ± 2.7 m.

CONCLUSIONS

We have devised a new method of assessing the precision of 3D locating systems, and we have used this method to test a pulse-flux magnetometer-based position locating system as part of an integrated 3D ultrasound imaging system. The results of applying the method to the POM system alone indicate that it performs well within the manufacturer's specifications. The performance of the system degrades smoothly as the position being measured begins to move beyond the specified 610 mm radius of operation.

When designing examination protocols, careful attention to the factors contributing to location uncertainty will improve the accuracy of 3D reconstructions. Several possible methods for reducing uncertainty include: realignment using anatomic or implanted fiducial marks, least squares techniques and fitting the raw data to geometric models, where applicable.

The results of this study have given us a better appreciation of the capabilities of our 3D ultrasound imaging system. Although the system is not sufficient for tomographic reconstructions requiring submillimeter alignment accuracies, such as multiangle tissue characterizations, the single-point position uncertainty of the system appears adequate for volume, surface area and length measurements of larger anatomic features.

REFERENCES

- Greenleaf, J. F.; Bahn, R. C. Clinical imaging with transmissive ultrasonic computerized tomography. *IEEE Trans. Biomed. Eng.* BME-28:177–185; 1981.
- King, D. L.; King, D. L. J.; Shao, M. Y. Evaluation of in vitro measurement accuracy of a three-dimensional ultrasound scanner. *J. Ultrasound Med.* 10:77–82; 1991.
- Levine, R. A.; Handschumacher, M. D.; Sanfilippo, A. J.; Hagege, A. A.; Harrigan, P.; Marshall, J. E.; Weyman, A. E. Three-dimensional echocardiographic reconstruction of the mitral valve, with implications for the diagnosis of mitral valve prolapse. *Circulation* 80:589–598; 1989.
- Martin, R. W.; Bashein, G.; Detmer, P. R.; Moritz, W. E. Ventricular volume measurement from a multiplanar transesophageal ultrasonic imaging system: An *in-vitro* study. *IEEE Trans. Biomed. Eng.* BME-37:442–449; 1990.
- Moritz, W. E.; Shreve, P. L.; Mace, L. E. Analysis of an ultrasonic spatial locating system. *IEEE Trans. Instrum. Meas.* IM-25:43–50; 1976.
- Moritz, W. E.; Shreve, P. L. A system for locating points, lines and planes in space. *IEEE Trans. Instrum. Meas.* IM-26:5–10; 1977.
- Moritz, W. E.; Pearlman, A. S.; McCabe, D. H.; Medema, D. K.; Ainsworth, A. K. An ultrasonic technique for imaging the ventricle in three dimensions and calculating its volume. *IEEE Trans. Biomed. Eng.* BME-30:482–491; 1983.
- Nerstrom, H.; Holm, H. H.; Christensen, N. E.; Movild, A. F.; Nolsoe, C. 3-dimensional ultrasound based demonstration of the posterior urethra during voiding combined with urodynamics. *Scand. J. Urol. Nephrol. Suppl.* 137:125–129; 1991.
- Schmitt, R. M.; Meyer, C. R.; Carson, P. L.; Samuels, B. I. Median and spatial low-pass filtering in ultrasonic computed tomography. *Med. Phys.* 11:767–771; 1984.
- Sohn, C.; Grotepass, J.; Schneider, W.; Funk, A.; Sohn, G. [Initial studies of three-dimensional imaging using ultrasound]. *Z. Geburtshilfe Perinatol.* 192:241–248; 1988a.
- Sohn, C.; Grotepass, J.; Schneider, W.; Sohn, G.; Funk, A. [Three-dimensional imaging in ultrasonic diagnosis. Initial results]. *Dtsch. Med. Wochenschr.* 113:1743–1747; 1988b.
- Sokolnikoff, I. S.; Redheffer, R. M. *Mathematics of physics and modern engineering*. New York: McGraw-Hill; 1958.
- Steinke, W.; Hennerici, M. Three-dimensional ultrasound imaging of carotid artery plaques. *J. Cardiovasc. Tech.* 8:15–22; 1989.
- Stone, M. A three-dimensional model of tongue movement based on ultrasound and x-ray microbeam data. *J. Acoust. Soc. Am.* 87:2207–2217; 1990.
- Watkin, K. L.; Rubin, J. M. Pseudo-three-dimensional reconstruction of ultrasonic images of the tongue. *J. Acoust. Soc. Am.* 85:496–499; 1989.

APPENDIX

RECURSIVE LEAST SQUARES POSITION DETERMINATION ALGORITHM

Evaluation of the POM system alone

The position locating system, operating in isolation, supplies the relative position and orientation of two rectangular axis systems: one defined by the transmitter's mechanical field coil configuration and the other by the receiver's pickup coil configuration. The system reports the x, y, z distance between the two axis systems' origins and the orientation of the axes with respect to each other. The transmitter, mounted on the examination table, was chosen to be the fixed frame of reference, with its axes labeled x, y and z . The receiver's axis system was labeled a, b and c (see Fig. 3).

If a point P is located a fixed distance from the receiver's origin, the x coordinate of the point, P_x , in the transmitter's axis system, can be calculated from the location of P in the receiver's coordinate system (A_a, A_b, A_c) using the location and orientation of the receiver in the transmitter's coordinate system as reported by the POM system:

$$P_x = R_x + A_a R_{ax} + A_b R_{bx} + A_c R_{cx}. \quad (1)$$

R_x is the x coordinate of the receiver's origin relative to the transmitter's origin. R_{ax} is the angle cosine that projects the receiver's a -axis onto the x -axis of the transmitter, with R_{bx} and R_{cx} defined in a like manner. The equations for calculating P_y and P_z are similar. In the fixed bead position experiment, the point P remains fixed relative to both the transmitter and the receiver, but the receiver is moved to many different positions and orientations relative to the transmitter, with the POM system data recorded at each point. Because A_a, A_b and A_c remain fixed, an overdetermined system of equations in matrix form can be set up from N multiple measurements to solve for P_x, P_y and P_z , which are also fixed:

$$\begin{bmatrix} P_{x1} \\ P_{y1} \\ P_{z1} \\ P_{x2} \\ \vdots \\ P_{xN} \end{bmatrix} = \begin{bmatrix} R_{x1} \\ R_{y1} \\ R_{z1} \\ R_{x2} \\ \vdots \\ R_{xN} \end{bmatrix} + \begin{bmatrix} R_{ax1} & R_{bx1} & R_{cx1} \\ R_{ay1} & R_{by1} & R_{cy1} \\ R_{az1} & R_{bz1} & R_{cz1} \\ R_{ax2} & R_{bx2} & R_{cx2} \\ \vdots & \vdots & \vdots \\ R_{axN} & R_{bxN} & R_{cxN} \end{bmatrix} \begin{bmatrix} A_a \\ A_b \\ A_c \end{bmatrix}, \quad (2)$$

or in abbreviated matrix notation:

$$\mathbf{P} = \mathbf{R}_p + \mathbf{R}_o \mathbf{A}. \quad (3)$$

Each triple (P_{xi}, P_{yi}, P_{zi}) in \mathbf{P} is an estimate of the fixed point's x , y and z location in the transmitter's axis system for the i th measurement, $i = 1, \dots, N$. \mathbf{R}_p and \mathbf{R}_o contain the receiver's position and orientation data, respectively, as supplied by the POM system, with each three consecutive rows containing the data from a single measurement. If the estimates have a reasonably uniform spatial distribution, their mean, $\bar{\mathbf{P}} = (\bar{P}_x, \bar{P}_y, \bar{P}_z)$, is the best estimate of the true location of the point relative to the transmitter, based on the set of POM measurements and the distance between the point and the receiver's origin, \mathbf{A} . For each measurement, the error distance between the measured and estimated true point location can be written:

$$\mathbf{P} - \bar{\mathbf{P}} = \begin{bmatrix} P_{x1} - \bar{P}_x \\ P_{y1} - \bar{P}_y \\ P_{z1} - \bar{P}_z \\ P_{x2} - \bar{P}_x \\ \vdots \\ P_{zN} - \bar{P}_z \end{bmatrix}. \quad (4)$$

The total squared error, L (a scalar), around the estimated true position is:

$$L = [\mathbf{P} - \bar{\mathbf{P}}]^T [\mathbf{P} - \bar{\mathbf{P}}] \\ = [\mathbf{R}_p + \mathbf{R}_o \mathbf{A} - \bar{\mathbf{P}}]^T [\mathbf{R}_p + \mathbf{R}_o \mathbf{A} - \bar{\mathbf{P}}]. \quad (5)$$

Once an estimate of $\bar{\mathbf{P}}$ is obtained using a given value of \mathbf{A} , a new value of \mathbf{A} can be calculated that minimizes L . The new value of \mathbf{A} is determined by the usual method: taking the derivative of L with respect to \mathbf{A} , setting it equal to zero, then solving for \mathbf{A} . The result is:

$$\mathbf{A} = (\mathbf{R}_o^T \mathbf{R}_o)^{-1} \mathbf{R}_o^T (\bar{\mathbf{P}} - \mathbf{R}_p). \quad (6)$$

Once a new value of \mathbf{A} has been calculated, a new set of position estimates, \mathbf{P} , can be made using the same set of POM measurements in \mathbf{R}_p and \mathbf{R}_o . This iterative process can be repeated until the total squared error converges to a minimum value. The final value of \mathbf{A} is the best estimate of the location of the point \mathbf{P} with respect to the receiver's origin, and the final value of $\bar{\mathbf{P}}$ is the best estimate of the point's location in transmitter coordinates for the set of measurements in \mathbf{R}_p and \mathbf{R}_o . The precision of the locating system is determined from the vector sum of the standard deviations of the individual x , y , z components of \mathbf{P} around $\bar{\mathbf{P}}$.

Evaluation of the combined POM and ultrasound imaging system

When using the POM system in conjunction with an ultrasound scanner to determine the location of feature points in space, the location of a feature point \mathbf{P} in the receiver axis system will vary depending on the location of \mathbf{P} in the image plane and the orientation of the scanhead's image plane with respect to the receiver's axis system. Calculation of the point's spatial location becomes a two-step process of mapping the image plane's 2D row-column axis system into the receiver's 3D axis system, then mapping this result into the transmitter's axis system. Let r and q represent the row and column locations, respectively, of a pixel J in the image, already corrected for aspect ratio distortion and millimeter scale factor. The matrix form of the equations to perform the two-step mapping is:

$$\begin{bmatrix} P_x \\ P_y \\ P_z \end{bmatrix} = \begin{bmatrix} R_x \\ R_y \\ R_z \end{bmatrix} + \begin{bmatrix} R_{ax} & R_{bx} & R_{cx} \\ R_{ay} & R_{by} & R_{cy} \\ R_{az} & R_{bz} & R_{cz} \end{bmatrix} \begin{bmatrix} S_a & S_{ra} & S_{qa} \\ S_b & S_{rb} & S_{qb} \\ S_c & S_{rc} & S_{qc} \end{bmatrix} \begin{bmatrix} 1 \\ J_r \\ J_q \end{bmatrix}, \quad (7)$$

or

$$\mathbf{P} = \mathbf{R}_p + \mathbf{R}_o \mathbf{S} \mathbf{J}, \quad (8)$$

where the elements of \mathbf{P} , \mathbf{R}_p and \mathbf{R}_o are the same as in eqns (2) and (3) above. \mathbf{J} contains the coordinates of the point \mathbf{P} in the ultrasound scanhead's image plane and \mathbf{S} is the matrix that maps the image plane's r and q axes into the receiver's a , b , c coordinate system. S_a , S_b and S_c are the distances from the image plane's r , q axis system origin to the receiver's origin. S_{ra} is the angle cosine that projects the image plane's row axis onto the receiver's a -axis, with S_{rb} and S_{rc} defined similarly. S_{qa} , S_{qb} and S_{qc} are the angle cosines projecting the image's column axis onto the receiver's axis system.

The form of eqn (8) is well suited for the task of rapidly mapping many points from the 2D image plane into the 3D space of the transmitter. However, another scalar loss function, L , must be defined, representing the total squared error, to implement an iterative procedure to calibrate the elements of \mathbf{S} and estimate the variability in locating \mathbf{P} . The minimization of L with respect to the elements of \mathbf{S} can be more easily accomplished by converting the matrix \mathbf{S} into a vector \mathbf{S}' and combining into one matrix both the point's location in the image, J_r and J_q , and the receiver's orientation values for that image, \mathbf{R}_o . The rearranged form for N points is:

$$\begin{bmatrix} P_{x1} \\ P_{y1} \\ P_{z1} \\ P_{x2} \\ \vdots \\ P_{zN} \end{bmatrix} = \begin{bmatrix} R_{x1} \\ R_{y1} \\ R_{z1} \\ R_{x2} \\ \vdots \\ R_{zN} \end{bmatrix} + \begin{bmatrix} R_{ax1} & R_{bx1} & R_{cx1} & R_{ax1}J_{r1} & R_{bx1}J_{r1} & R_{cx1}J_{r1} & R_{ax1}J_{q1} & R_{bx1}J_{q1} & R_{cx1}J_{q1} \\ R_{ay1} & R_{by1} & R_{cy1} & R_{ay1}J_{r1} & R_{by1}J_{r1} & R_{cy1}J_{r1} & R_{ay1}J_{q1} & R_{by1}J_{q1} & R_{cy1}J_{q1} \\ R_{az1} & R_{bz1} & R_{cz1} & R_{az1}J_{r1} & R_{bz1}J_{r1} & R_{cz1}J_{r1} & R_{az1}J_{q1} & R_{bz1}J_{q1} & R_{cz1}J_{q1} \\ R_{ax2} & R_{bx2} & R_{cx2} & R_{ax2}J_{r2} & R_{bx2}J_{r2} & R_{cx2}J_{r2} & R_{ax2}J_{q2} & R_{bx2}J_{q2} & R_{cx2}J_{q2} \\ \vdots & \vdots & \vdots & \vdots & \vdots & \vdots & \vdots & \vdots & \vdots \\ R_{azN} & R_{bzN} & R_{czN} & R_{azN}J_{rN} & R_{bzN}J_{rN} & R_{czN}J_{rN} & R_{azN}J_{qN} & R_{bzN}J_{qN} & R_{czN}J_{qN} \end{bmatrix} \begin{bmatrix} S_a \\ S_b \\ S_c \\ S_{ra} \\ S_{rb} \\ S_{rc} \\ S_{qa} \\ S_{qb} \\ S_{qc} \end{bmatrix} \quad (9)$$

or more succinctly,

$$\mathbf{P} = \mathbf{R}_p + \hat{\mathbf{R}}_o \mathbf{S}'. \quad (10)$$

Three constraints must be adjoined to this system of equations to prevent distortion by ensuring that the transformation of the image plane's axes into the receiver's axis system is orthogonal and scaled to unity. These constraints can be written in vector form as:

$$[S_{ra}, S_{rb}, S_{rc}][S_{ra}, S_{rb}, S_{rc}]^T - 1 = 0, \quad (11)$$

$$[S_{qa}, S_{qb}, S_{qc}][S_{qa}, S_{qb}, S_{qc}]^T - 1 = 0, \quad \text{and} \quad (12)$$

$$[S_{ra}, S_{rb}, S_{rc}][S_{qa}, S_{qb}, S_{qc}]^T = 0. \quad (13)$$

The first two constraints force unity scaling, preventing magnification or reduction of the image's scale along the rows or columns, when mapped into the receiver's axis system. The constraint in eqn

(13) forces the image plane's row and column axes to be orthogonal during conversion into the receiver axis system. The Ascension Technology POM system forces similar constraints for the receiver to transmitter axis mapping within its hardware.

To incorporate the constraints, the iterative algorithm solved above for the POM system alone must be modified slightly. The constraint equations were linearized using a Taylor series expansion around the previous iteration's estimate of \mathbf{S}' , truncated at the first order derivative. The method of Lagrange multipliers (Sokolnikoff and Redheffer 1958) was then used to solve for an \mathbf{S}' that minimized the squared error of the location scatter around the single point, subject to the linearized constraints equations. The linearized forms of eqns (11)–(13) are:

$$\begin{bmatrix} 0 & 0 & 0 & 2S_{rao} & 2S_{rbo} & 2S_{rco} & 0 & 0 & 0 \\ 0 & 0 & 0 & 0 & 0 & 0 & 2S_{qao} & 2S_{qbo} & 2S_{qco} \\ 0 & 0 & 0 & S_{qao} & S_{qbo} & S_{qco} & S_{rao} & S_{rbo} & S_{rco} \end{bmatrix}$$

$$2(S_{rao}S_{ra} + S_{rbo}S_{rb} + S_{rco}S_{rc}) - (S_{rao}^2 + S_{rbo}^2 + S_{rco}^2) - 1 = 0, \quad (14)$$

$$2(S_{qao}S_{qa} + S_{qbo}S_{qb} + S_{qco}S_{qc}) - (S_{qao}^2 + S_{qbo}^2 + S_{qco}^2) - 1 = 0, \quad (15)$$

$$S_{qao}S_{ra} + S_{rao}S_{qa} + S_{qbo}S_{rb} + S_{rbo}S_{qb} + S_{qco}S_{rc} + S_{rco}S_{qc} - (S_{rao}S_{qao} + S_{rbo}S_{qbo} + S_{rco}S_{qco}) = 0, \quad (16)$$

where S_{rao} , S_{rbo} , S_{rco} , S_{qao} , S_{qbo} and S_{qco} are the values of S_{ra} , S_{rb} , S_{rc} , S_{qa} , S_{qb} and S_{qc} , respectively, from the previous iteration's estimate of \mathbf{S}' .

These can be combined into a matrix form incorporating the unknown vector \mathbf{S}' we are solving for:

$$\begin{bmatrix} S_a \\ S_b \\ S_c \\ S_{ra} \\ S_{rb} \\ S_{rc} \\ S_{qa} \\ S_{qb} \\ S_{qc} \end{bmatrix} - \begin{bmatrix} (S_{rao}^2 + S_{rbo}^2 + S_{rco}^2 + 1) \\ (S_{qao}^2 + S_{qbo}^2 + S_{qco}^2 + 1) \\ (S_{rao}S_{qao} + S_{rbo}S_{qbo} + S_{rco}S_{qco}) \end{bmatrix} = 0, \quad (17)$$

or

$$\mathbf{CS}' - \mathbf{D} = 0. \quad (18)$$

Using the Lagrange multiplier method we find the values in \mathbf{S}' and $\boldsymbol{\lambda}$ that minimize the squared error using:

$$L = [\mathbf{P} - \bar{\mathbf{P}}]^T[\mathbf{P} - \bar{\mathbf{P}}] = [\mathbf{R}_p + \hat{\mathbf{R}}_0\mathbf{S}' - \bar{\mathbf{P}}]^T[\mathbf{R}_p + \hat{\mathbf{R}}_0\mathbf{S}' - \bar{\mathbf{P}}] - \boldsymbol{\lambda}^T[\mathbf{CS}' - \mathbf{D}]. \quad (19)$$

If the linearized constraints in the last term are ideally met, no additional squared error will be added. The error is minimized by taking the derivatives of L with respect to \mathbf{S}' and $\boldsymbol{\lambda}$, setting the resulting equations equal to zero and solving for \mathbf{S}' and $\boldsymbol{\lambda}$. By using partitioned matrices, where the elements of the matrix equations

involving $\boldsymbol{\lambda}$, \mathbf{C} and \mathbf{D} have been appended onto the equations for \mathbf{P} , $\hat{\mathbf{R}}$ and \mathbf{S}' , both sets of equations can be combined into a more compact notation and solved simultaneously. The combined matrix equations to solve simultaneously for \mathbf{S}' and $\boldsymbol{\lambda}$ are:

$$[\mathbf{S}'^T | \boldsymbol{\lambda}^T] = [2(\mathbf{P} - \hat{\mathbf{R}}_p)^T \hat{\mathbf{R}}_0 | -\mathbf{D}^T] \left[\frac{2\hat{\mathbf{R}}_0^T \hat{\mathbf{R}}_0}{\mathbf{C}} \middle| \frac{\mathbf{C}^T}{\mathbf{0}} \right]^{-1}. \quad (20)$$

Using this equation to solve for the vector \mathbf{S}' in place of eqn. (6) solving for vector \mathbf{A} , the iterative algorithm is run in exactly the same manner to solve for the position of the target point, calculating the best values for \mathbf{S}' and the scatter around the target point at the same time. Rearrangement of the values in \mathbf{S}' to matrix form then permits the use of eqn. (8) to calculate the location of any point in three-space, given the location of the point in the image plane and the plane's position and orientation according to the POM system.